1 # Supporting Information For

2 # Ultrafast Electrical Charge Injection in Operating Perovskite Light-
3 # Emitting Diodes by Infrared Optical Control

4 *Ruoyu Gao[1], Zhongcheng Yuan[2,3], Bin Yang[1], Longren Li[1], Marie Houot[1],*
5 *Mengyuan Huang[1], Ben Spencer[4], Seonghyeok Park[5], Nicola Gasparini[1],*
6 *Henry J. Snaith[2,*], Ziming Chen[1,6,*], and Artem A. Bakulin[1,*]*
7

8 [1] Department of Chemistry and Centre for processable Electronics, Molecular Sciences Research Hub, Imperial
9 College London, London W12 0BZ, United Kingdom.

10 [2] Clarendon Laboratory, Department of Physics, University of Oxford, Oxford OX1 3PU, United Kingdom.

11 [3] School of Sustainable Energy and Resources, Nanjing University, Suzhou, People's Republic of China

12 [4] Manchester University

13 [5] London South Bank University

14 [6] Department of Mechanical Engineering, The University of Hong Kong, Hong Kong, 999077, China

15

16 **This file includes:**

17 **Supplementary Figures S1-S18**

18 Figure S1: *Ultraviolet photoelectron spectroscopy of perovskite and ZnO/PEIE layers.*

19 *Figure S2: UV-VIS spectra of ZnO, TFB and $CsPbI_{3-x}Br_x$.*

20 *Figure S3: Response time of the photomultiplier tube detector.*

21 *Figure S4: Device properties of the PeLED used.*

22 *Figure S5: J-V curve and steady-state charge-induced absorption spectrum of the device with*
23 *TFB or ZnO/PEIE layer only.*

24 *Figure S6: Temporal evolution of femtosecond transient absorption spectroscopy signal (fs-*
25 *TAS) in PeLED device without electrical pump bias.*

26 *Figure S7: fs-TAS spectra of different device-layer stacks.*

27 *Figure S8: Injection-time dependence push-induced signals in PeLED devices.*

28 *Figure S9: Controlling PeLED device with hole-blocking layers with IR assisted electrical*
29 *injection.*

30 *Figure S10: Temporal evolution of Epump-IRpush-VISprobe spectrum with different pump-push time at a push-probe time of 20 to 60 ps averaged in the device with hole-blocking layers.*

32 *Figure S11: Temporal evolution of Epump-IRpush-VISprobe spectrum with different pump-push time at a push-probe time of 20 to 60 ps averaged in the device with electron-blocking layers.*

35 *Figure S12: Push effect on EL at Pump-off conditions for PeLED device.*

36 *Figure S13: Timing reference for the IR push pulse measured using an IR-viewing card.*

37 *Figure S14 Control fs-TAS measurement on multi-stack devices at different conditions.*

38 *Figure S15: Electrochemical impedance spectroscopy (EIS) results of the PeLED device.*

39 *Figure S16: Overshot effect captured in time-resolved electroluminescence (TREL) at biases with different pulse durations.*

41 *Figure S17: fs-TAS on TFB, ZnO and $CsPbI_{3-x}Br_x$ films.*

42 *Figure S18:* Simulated spatiotemporal carrier-density maps in the Au/TFB/$CsPbBrI_2$/ZnO/ITO device under electrical excitation, with and without the IR push pulse.

45 **Supplementary note 1: Impedance spectroscopy of the PeLED devices**

46 **Supplementary Note 2: Simulation Result**

47 **Supplementary Note 3: Self-Consistent Full-Device Drift-Diffusion Model for Push-Assisted Charge Injection and the ΔEL Response**

49 **Table S1: Fixed layer properties used in the full-device simulation.**

50 **Table S2: Fixed experimental timing and numerical settings used in the transient simulations.**

51

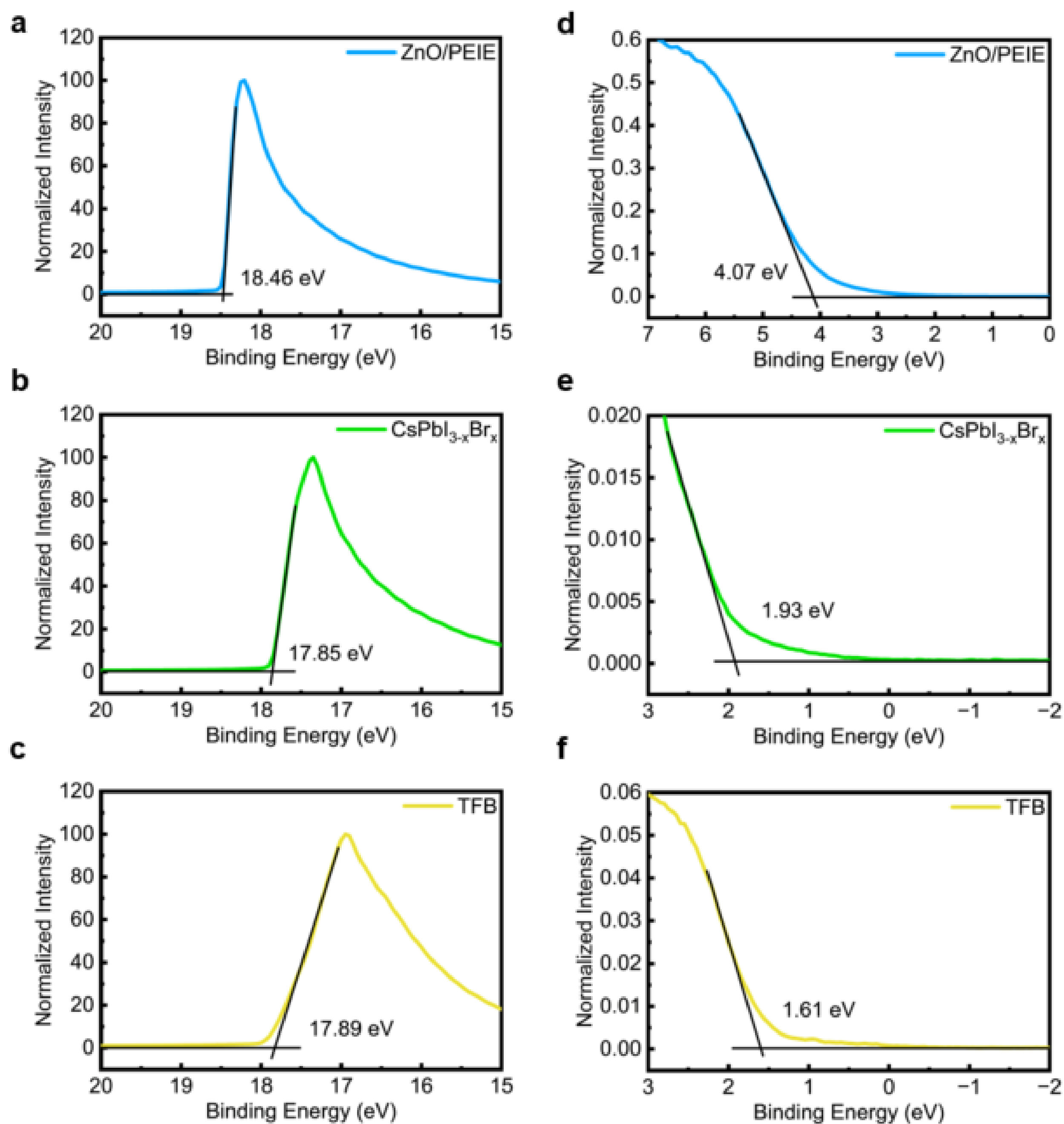

52

53 ***Figure S1. Ultraviolet photoelectron spectroscopy of perovskite and ZnO/PEIE layers.*** *The*
54 *samples are excited with a He I radiation source with photon energy of 21.22 eV. The calculated*
55 *valance bands were -6.83 eV, -5.30 eV and -4.94 eV for ZnO/PEIE,* $CsPbI_{3-x}Br_x$*, and TFB devices,*
56 *respectively.*

57

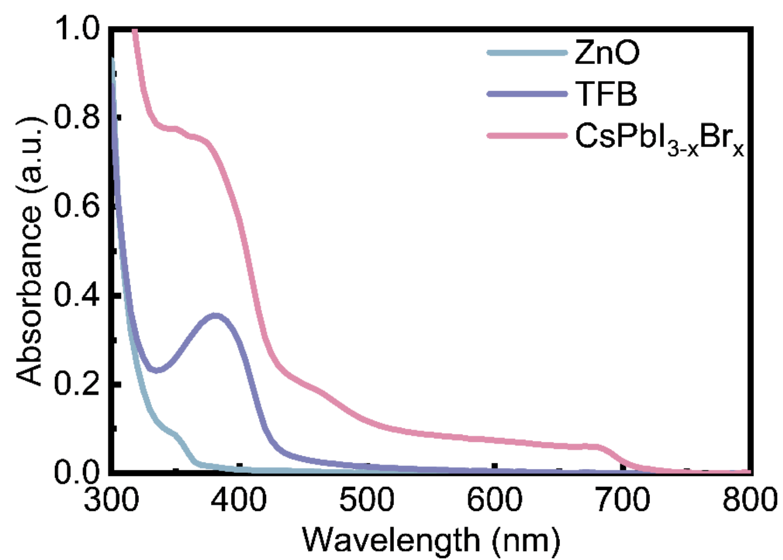

58

59 ***Figure S2. UV-VIS spectra of ZnO, TFB and $CsPbI_{3-x}Br_x$.***

60

61

62

63

64

65

66

67

68

69

70

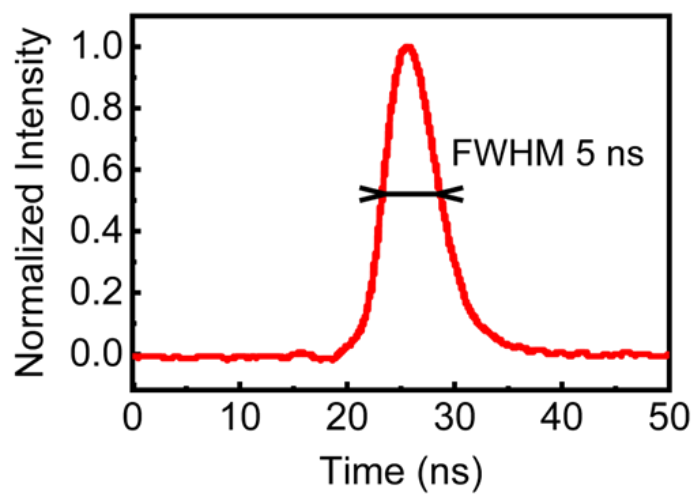

71

72 ***Figure S3. Response time of the photomultiplier tube detector.*** *It was used to collect all the signals*
73 *in this work. The signal was captured by the oscilloscope*

74

75

76

77

78

79

80

81

82

83

84

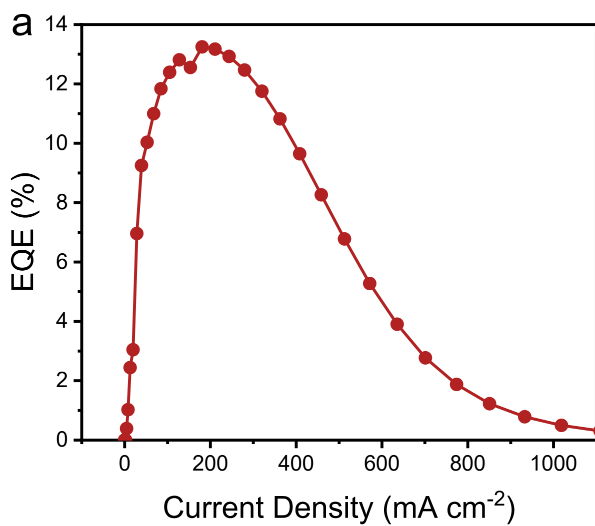

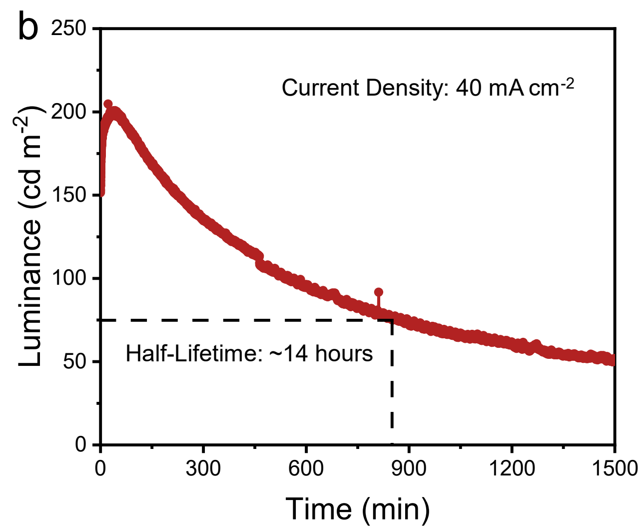

85

86 ***Figure S4. Device properties of the PeLED used.*** *(**a**) Current density versus EQE curve. (**b**) Device*
87 *operational stability under constant current injection of 40 mA cm*$^{-2}$.

88

89

90

91

92

93

94

95

96

97

98

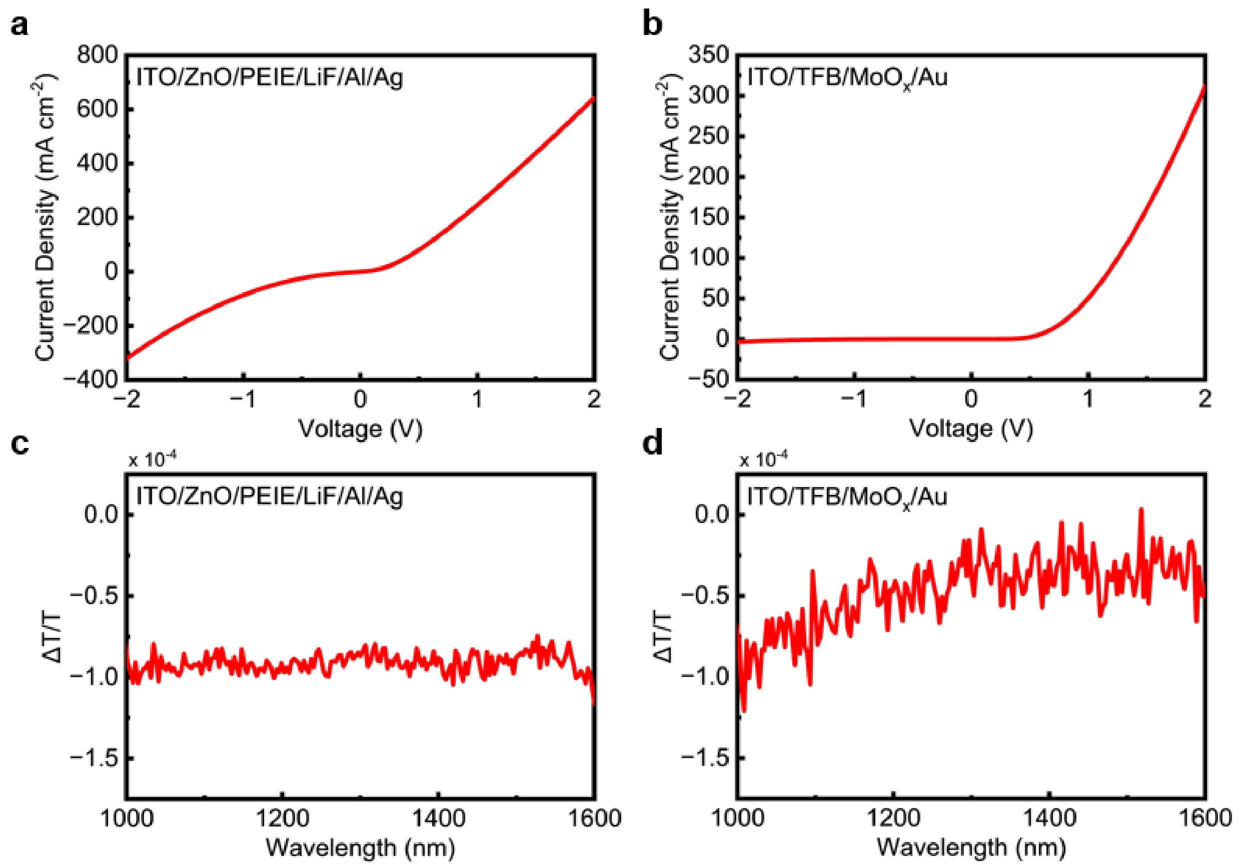

99

100 ***Figure S5. J-V curve and steady-state charge-induced absorption spectrum of the device with***
101 ***TFB or ZnO/PEIE layer only. a*** *The electron-only device of ITO/ZnO/LiF/Al/Ag is quasi-ohmic.* ***b***
102 *the hole-only device of ITO/TFB/MoO$_x$/Au functions as a diode.* ***c*** *Steady-state electron absorption*
103 *spectrum of the ITO/ZnO/LiF/Al/Ag device at 2 V.* ***d*** *Steady-state hole absorption spectrum of*
104 *ITO/TFB/MoO$_x$/Au device at 2 V.*

105

106

107

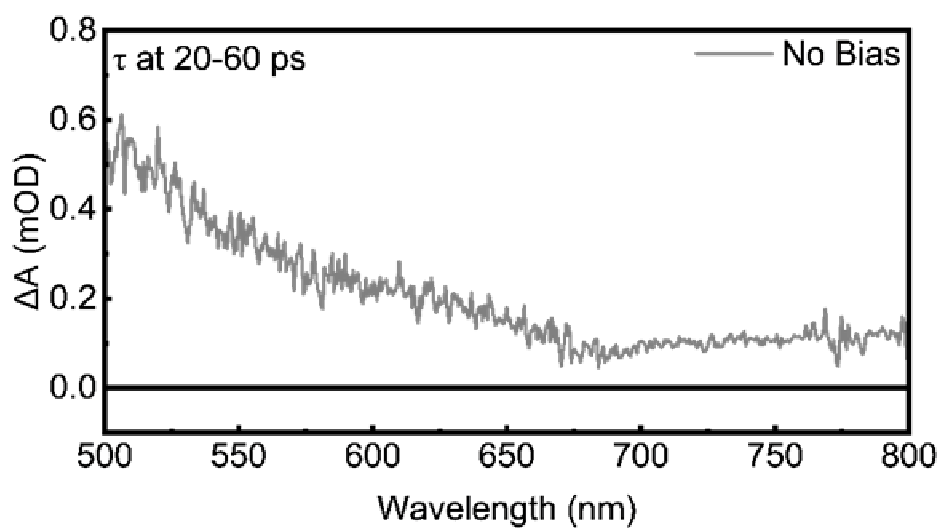

108

109 ***Figure S6. Temporal evolution of femtosecond transient absorption spectroscopy signal (fs-TAS)***
110 ***in PeLED device without electrical pump bias.*** *The excitation is 1300 nm with a fluence of 1.0 mJ*
111 *cm*$^{-2}$*. In the absence of bias, the signal raised from the heating of Au electrode and the characteristic*
112 *band-edge response from the perovskite layer is absent.*

113

114

115

116

117

118

119

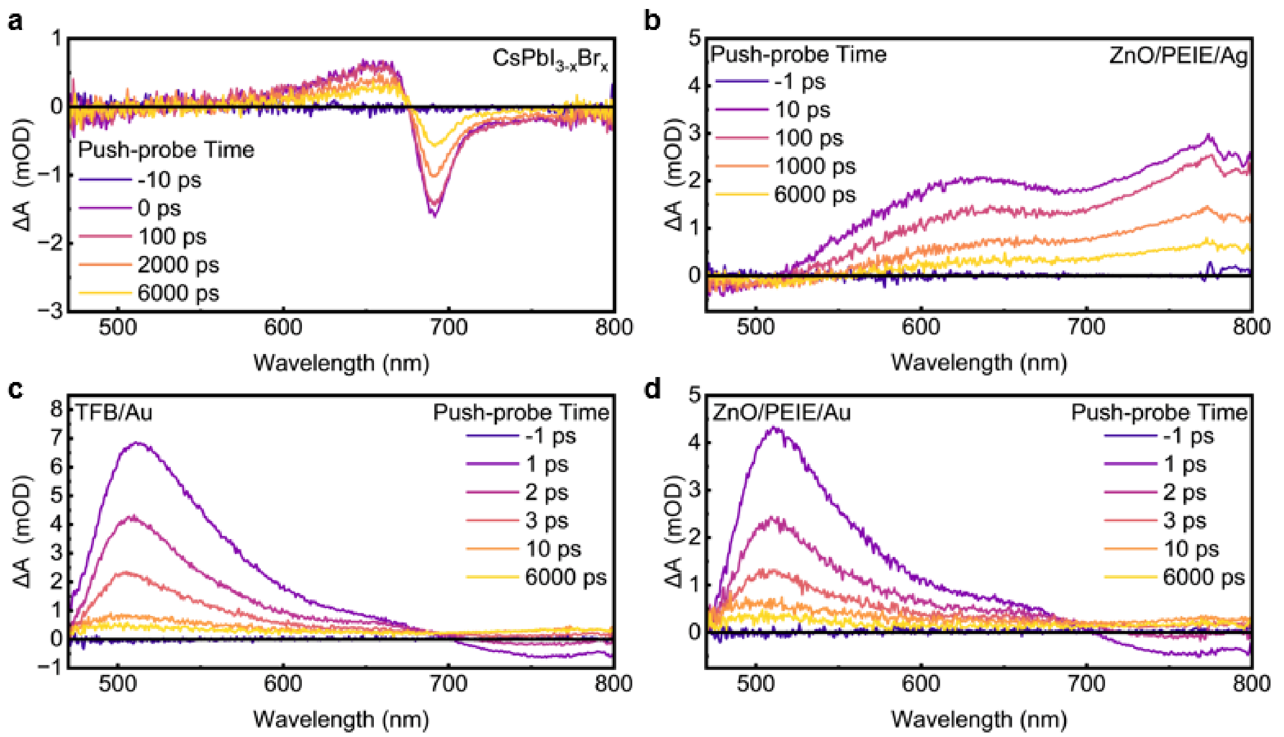

120

121 ***Figure S7. fs-TAS spectra of different device-layer stacks.*** *Temporal evolution of fs-TAS spectrum*
122 *in* ***(a)*** *$CsPbI_{3-x}Br_x$ film,* ***(b)*** *ZnO/PEIE/Ag tri-layer,* ***(c)*** *TFB/Au bi-layer,* ***(d)*** *ZnO/PEIE/Au tri-layer.*
123 *The push wavelength is 1300 nm with the fluence of 10.6 mJ cm^{-2} in $CsPbI_{3-x}Br_x$ film (to trigger multi-*
124 *photon absorption), 6.4 mJ cm^{-2} in ZnO/PEIE/Ag, 8.8 mJ cm^{-2} in TFB/Au, and 6.4 mJ cm^{-2} in*
125 *ZnO/PEIE/Au. Comparing the features in different samples suggests that the photoinduced*
126 *absorption (PIA) signal around 510 nm comes from the Au electrode.*

127

128

129

130

131

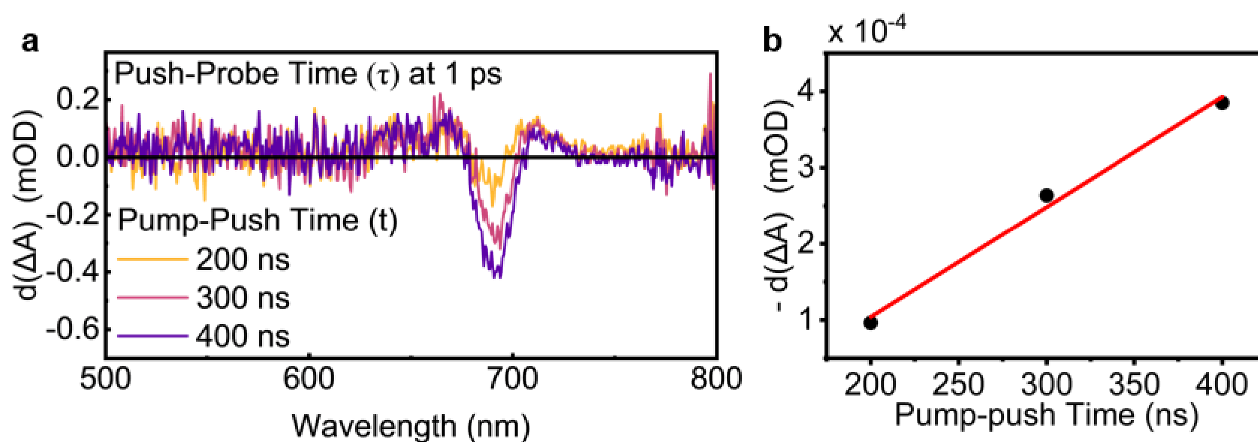

Figure S8. Injection-time dependence push-induced signals in PeLED devices. a *Temporal spectrum of d(ΔA) at different pump-push time. It suggests that when gradually increasing pump-push time, i.e., allowing more time for charge injections from electrical pulsed bias before push arriving, more accumulated carriers can be pushed into perovskite layers to contribute to push-induced signals. The pump source has a voltage of 5 V and a duration of 500 ns. The push light has a wavelength of 1300 nm and a fluence of 1.0 mJ* cm^{-2}. ***b*** *The average absolute value from 688 nm to 693 nm of d(ΔA) at different pump-push time. The trend shows that d(ΔA) has a linear relationship with pump-push time.*

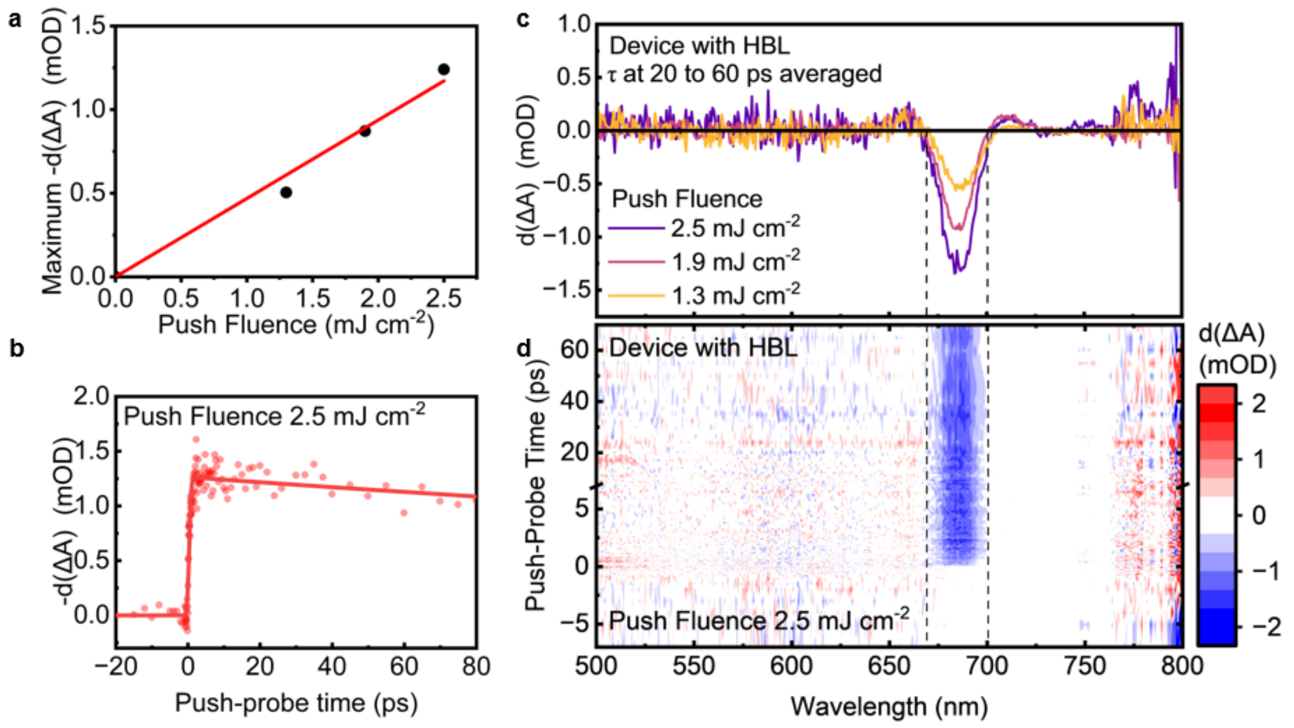

146

147 ***Figure S9. Controlling PeLED device with hole-blocking layers with IR assisted electrical***
148 ***injection. a*** *Push fluence dependence of maximum IR-induced signals.* ***b*** *Kinetics of push-induced*
149 *signals under a push wavelength of 1300 nm and a fluence of 2.5 mJ cm*$^{-2}$. ***c*** *Push fluence dependence*
150 *of push-induced signals at an averaged push-probe time of 20 to 60 ps.* ***d*** *Spectrogram of push-*
151 *induced signals at a push fluence of 2.5 mJ cm*$^{-2}$.

152

153

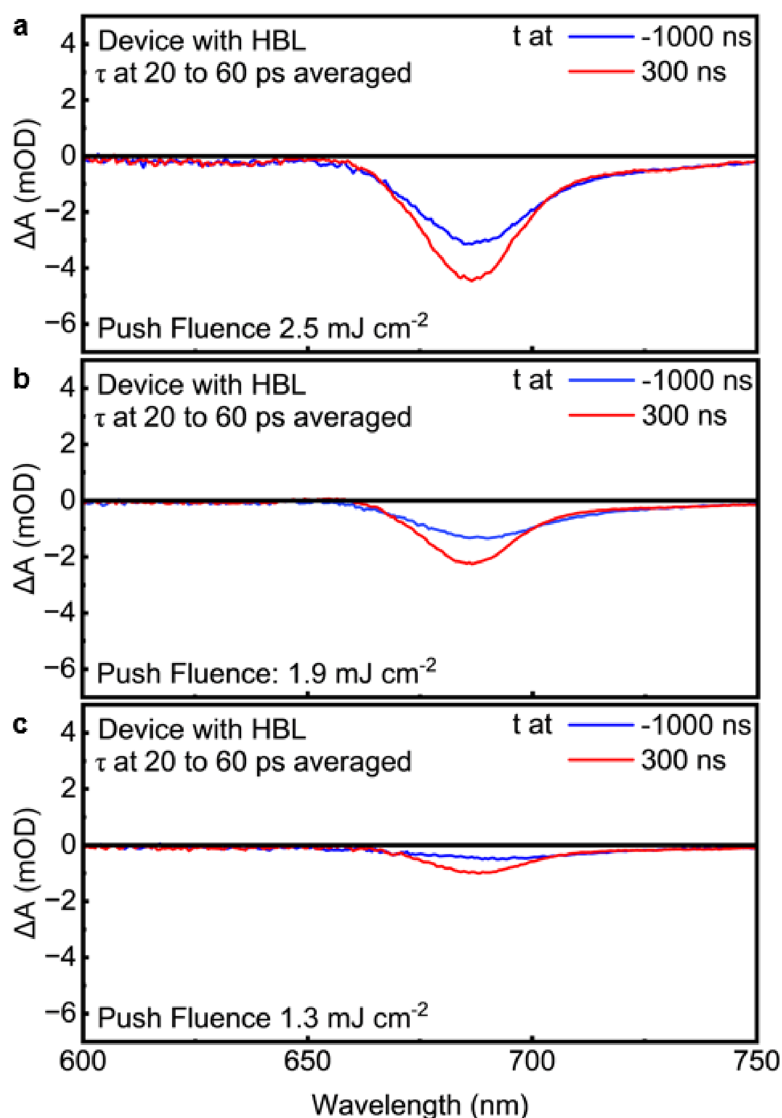

154 ***Figure S10. Temporal evolution of Epump-IRpush-VISprobe spectrum with different pump-push***
155 ***time at a push-probe time of 20 to 60 ps averaged in the device with hole-blocking layers.*** *The push*
156 *source is 1300 nm with fluence of (**a**) 2.5 mJ cm^{-2}, (**b**) 1.9 mJ cm^{-2}, (**c**) 1.3 mJ cm^{-2}. The electrical*
157 *pump is a pulsed bias with the voltage of 5 V and the duration of 500 ns. Devices containing blocking*
158 *layers showed lower signal-to-noise ratios than the standard PeLEDs, so higher IR push fluences*
159 *were required to resolve the field-dependent injection signal. Under these conditions, a weak band-*
160 *edge-like background is also observed at negative pump–push delay, where the IR pulse arrives before*
161 *the electrical bias pulse. This background may arise from weak multiphoton excitation of the*
162 *perovskite layer enhances by additional blocking-layer interfaces. The injection-related contribution*
163 *was therefore identified from the systematic increase of the band-edge bleach at positive pump–push*
164 *delay, where electrically accumulated carriers are present and can be perturbed by the IR push pulse.*

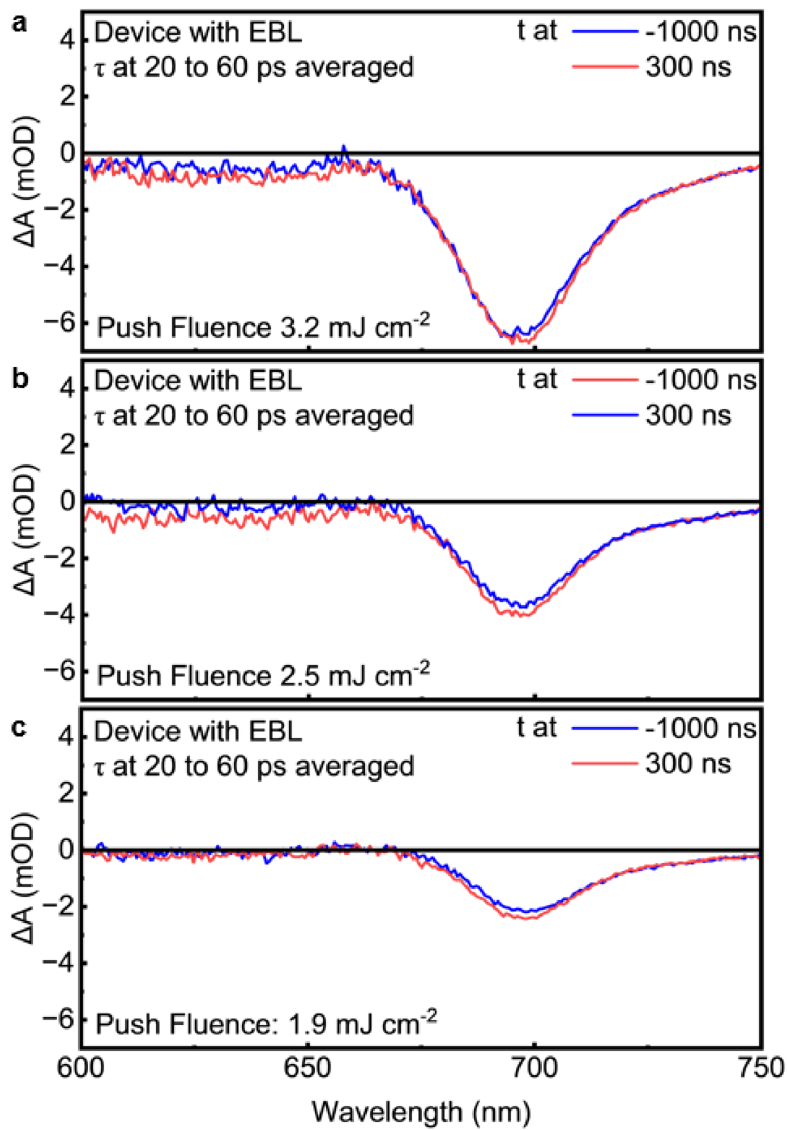

165

166 ***Figure S11. Temporal evolution of Epump-IRpush-VISprobe spectrum with different pump-push***
167 ***time at a push-probe time of 20 to 60 ps averaged in the device with electron-blocking layers.*** *The*
168 *push source is 1300 nm at an IR push fluence of (**a**) 3.2 mJ cm^{-2}, (**b**) 2.5 mJ cm^{-2}, (**c**) 1.9 mJ cm^{-2}. The*
169 *electrical pump is a pulsed bias with the voltage of 5 V and the duration of 500 ns. Devices containing*
170 *blocking layers showed lower signal-to-noise ratios than the standard PeLEDs, so higher IR push*
171 *fluences were required to resolve the field-dependent injection signal. Under these conditions, a weak*
172 *band-edge-like background is also observed at negative pump–push delay, where the IR pulse arrives*
173 *before the electrical bias pulse. This background may arise from weak multiphoton excitation of the*
174 *perovskite layer enhances by additional blocking-layer interfaces. The injection-related contribution*
175 *was therefore identified from the systematic increase of the band-edge bleach at positive pump–push*
176 *delay, where electrically accumulated carriers are present and can be perturbed by the IR push pulse.*

177

178

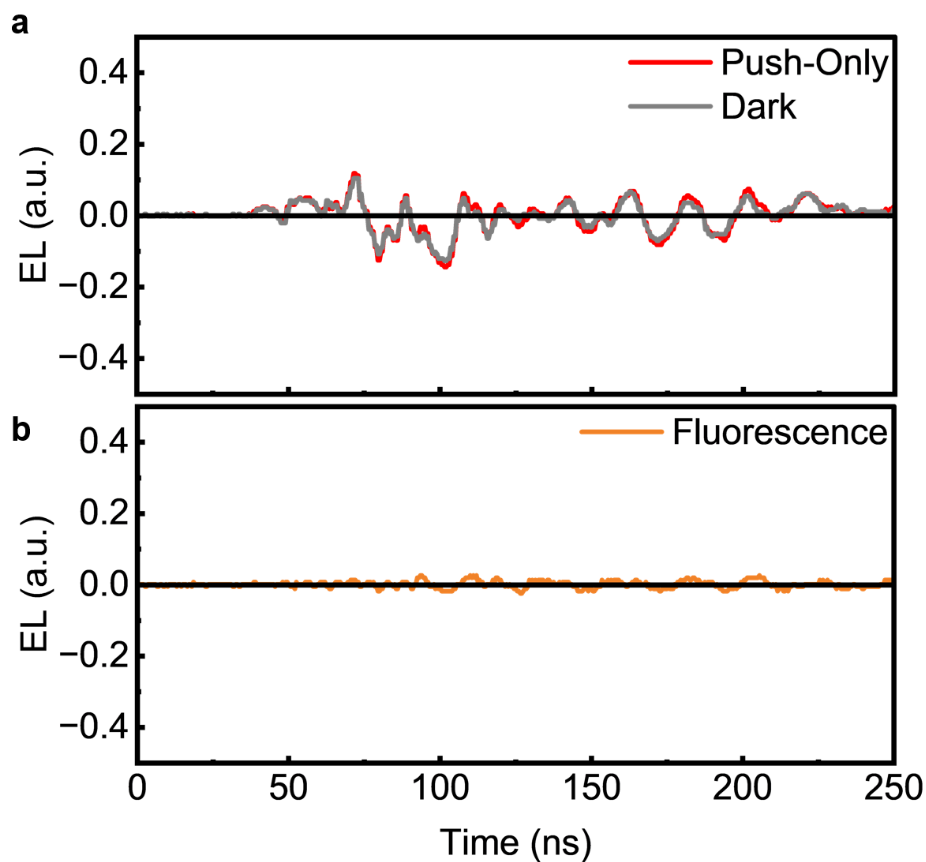

179

180 ***Figure S12. Push effect on EL at Pump-off conditions for PeLED device. a*** *Push-only and dark EL*
181 *signal and detected by PMT and oscilloscope. The push wavelength and fluence are 1064 nm and*
182 *11.1 mJ cm^{-2} respectively.* ***b*** *Difference between 'push-only' and 'dark' signals. This shows that IR*
183 *push itself does not generate PL/EL signals.*

184

185

186

187

188

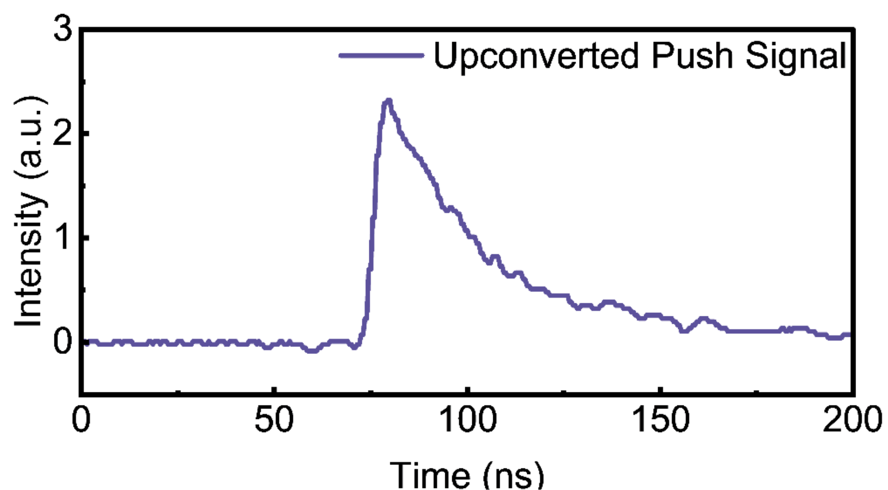

189 ***Figure S13. Timing reference for the IR push pulse measured using an IR-viewing card***. *The 1064*
190 *nm push pulse was blocked from directly reaching the detector. To determine its arrival time, an IR-*
191 *viewing card was placed at the sample position, where the incident IR pulse generated visible*
192 *emission through up-conversion/fluorescence from the card. This visible signal was detected with the*
193 *same photomultiplier/oscilloscope setup used for the time-resolved EL measurements. The rising edge*
194 *of the detected signal therefore provides an approximate timing reference for the arrival of the IR*
195 *push pulse at the sample position. The push wavelength and fluence were 1064 nm and 11.1 mJ cm^{-2},*
196 *respectively.*

197

198

199

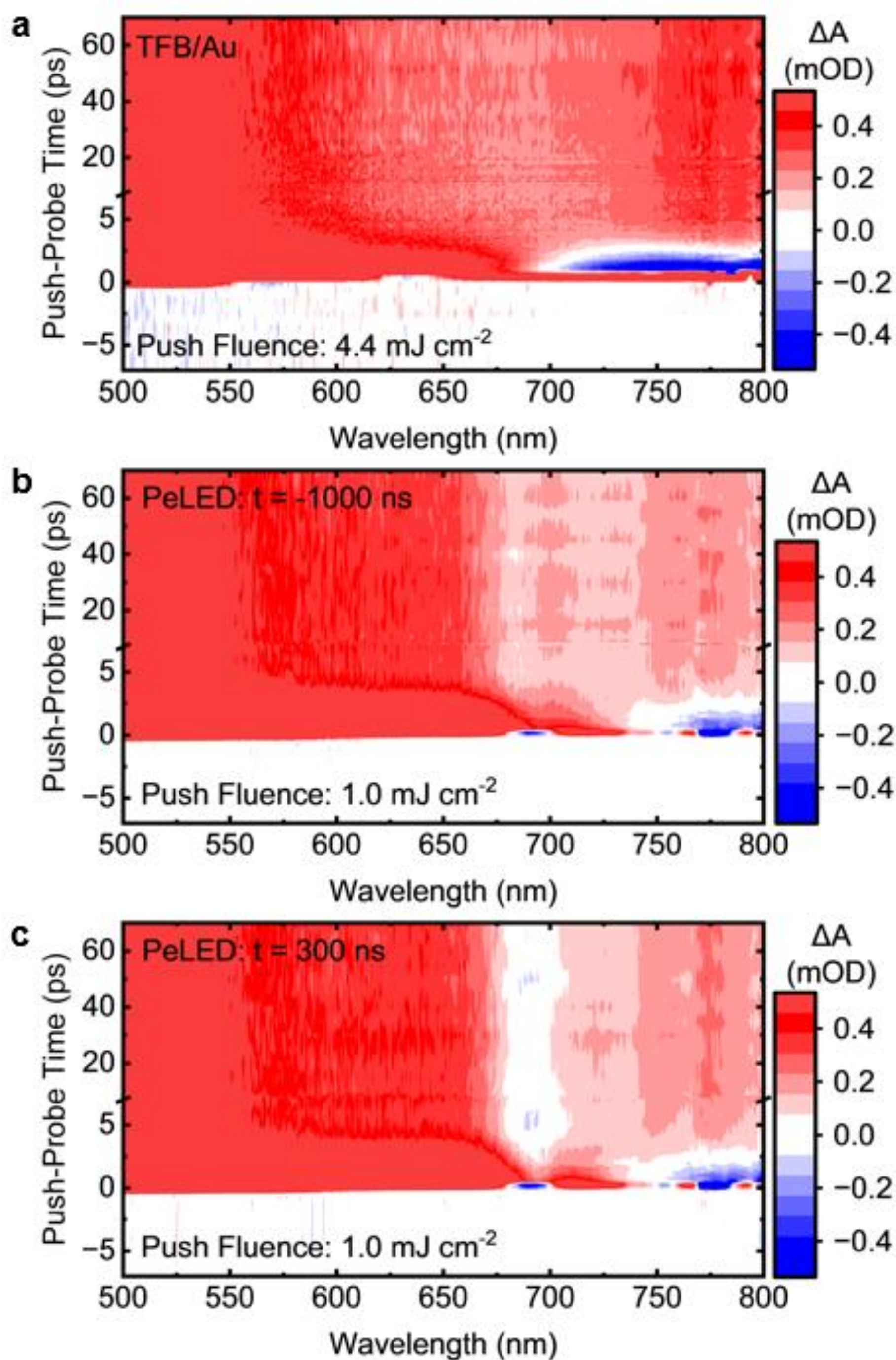

200

201 ***Figure S14. Control fs-TAS measurement on multi-stack devices at different conditions. a*** *fs-TAS*
202 *on TFB/Au bi-layer under no bias condition. The push beam has a wavelength of 1300 nm and a*
203 *fluence of 4.4 mJ cm^{-2}.* ***b*** *a fs-TAS on PeLED under an electrical pump (5 V, duration 500 ns) at pump-*
204 *push time of -1000 ns. The push beam has a wavelength of 1300 nm and a fluence of 1.0 mJ cm^{-2}.* ***c*** *a*
205 *fs-TAS on PeLED under an electrical pump (5 V, duration 500 ns) at a pump-push time of 300 ns. The*
206 *push beam has a wavelength of 1300 nm and a fluence of 1.0 mJ cm^{-2}.*

207

208

Supplementary note 1. Impedance spectroscopy of the PeLED devices.

Electrical impedance spectroscopy was performed to characterise the conventional electrical response of the PeLED device under different forward-bias conditions (Fig. S15). The impedance was measured from 1.0 to 3.5 V, covering both the sub-threshold regime and the regime after EL turn-on, which occurs at approximately 2 V. The extracted capacitance shows a strong dependence on both frequency and applied bias. At low bias, before turn-on, the device exhibits a very large low-frequency capacitance, consistent with the accumulation of charge at internal interfaces and/or slow redistribution processes in the device stack. At high frequencies, however, the capacitance converges towards a bias-independent value of approximately 1–2 nF. This value is close to the geometrical capacitance estimated from the device area and thickness, supporting the interpretation that the high-frequency response is dominated by the physical capacitance of the device stack rather than by slow interfacial charging processes. Using the measured high-frequency imaginary impedance, the geometrical capacitance was estimated as $C_g = 1/(2\pi f(-Z'')) \approx 1.25nF$. A similar value is obtained from the parallel-plate estimate, $C = \varepsilon\varepsilon_0 A/d$, using a device area of 4 mm², an active stack thickness of approximately 375 nm, and a relative dielectric constant of $\varepsilon \sim 20$, which gives $C \approx 1.9nF$.

The Nyquist plots further show a strong reduction in the characteristic time after device turn-on. Below turn-on, at 1.0 and 1.5 V, the impedance arcs are very large, indicating a high device resistance and slow electrical relaxation. The characteristic times extracted from the impedance spectra are 51.7 ms at 1.0 V and 719 μs at 1.5 V. Once the device reaches the EL operating regime, the impedance arcs become much smaller and the characteristic time decreases rapidly with increasing bias: 19.4 μs at 2.0 V, 7.1 μs at 2.5 V, 2.8 μs at 3.0 V, and 1.4 μs at 3.5 V. This trend is consistent with the opening of an efficient injection/recombination pathway after turn-on, which reduces the differential resistance of the device and accelerates the macroscopic electrical response. At the highest bias, the extracted characteristic time approaches the value expected from a simple RC estimate. Taking $C_g \approx 1.25nF$ and the high-frequency real impedance including the 50 Ω load resistance gives RC $\approx 223ns$, corresponding to a rise time of approximately $5RC \approx 1.1$ μs. This is close to the measured characteristic time of 1.4 μs at 3.5 V, indicating that under high forward bias the macroscopic electrical response of the device approaches an RC-limited regime.

This slow electrical relaxation is consistent with the time-resolved EL measurements under pulsed bias. As the electrical pulse duration is increased from 100 to 220 ns, the EL transient progressively grows and approaches a quasi-steady response only for pulse durations of approximately 200 ns and longer, indicating that the injected carrier population and associated space-charge distribution require hundreds of nanoseconds to become fully established during normal electrical operation.

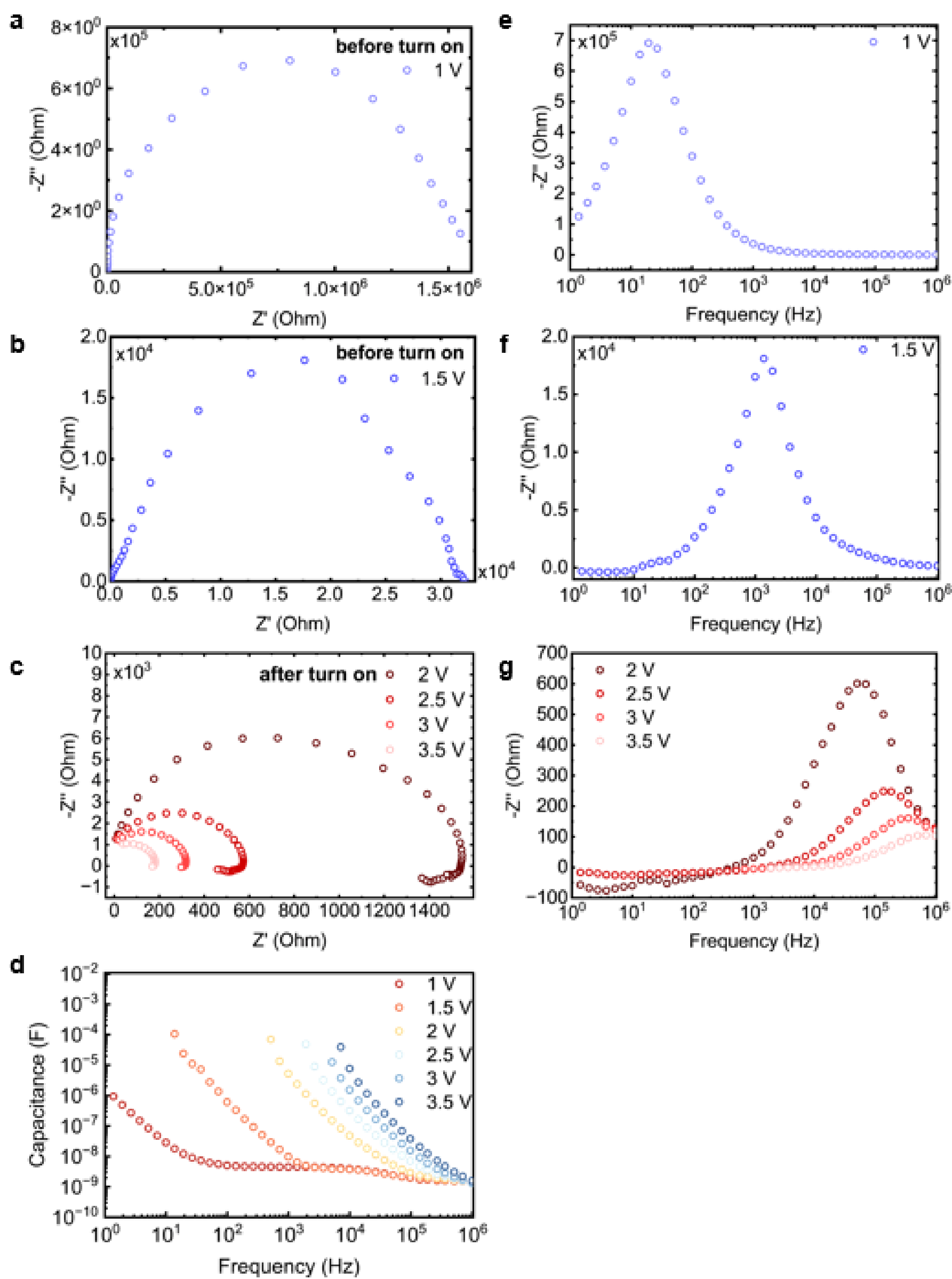

242

243 ***Figure S15. Electrochemical impedance spectroscopy (EIS) results of the PeLED device.***

244

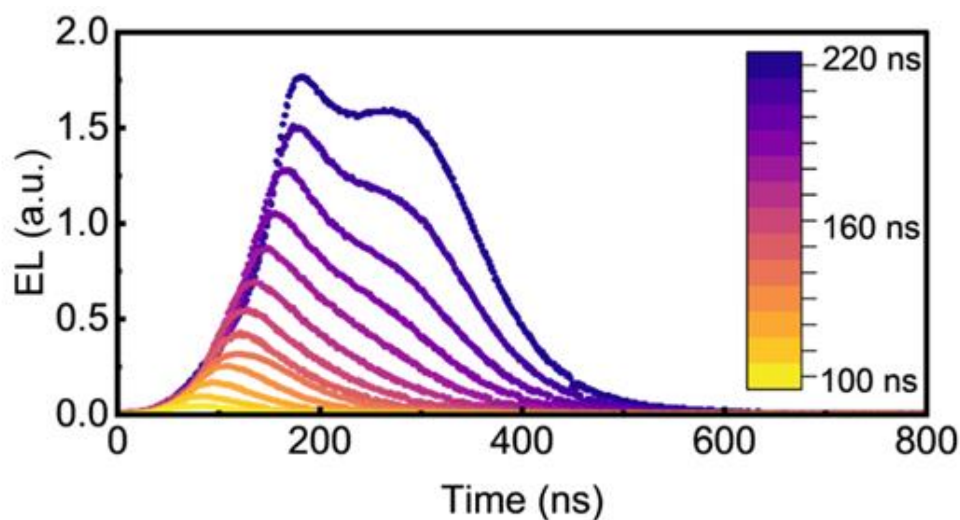

245

246 ***Figure S16. Overshot effect captured in time-resolved electroluminescence (TREL) at biases with***
247 ***different pulse durations.*** *The applied bias is fixed with the voltage of 5 V. The pulse duration*
248 *increased from 100 ns to 220 ns with the interval of 10 ns. As the pulse duration is increased, an*
249 *overshoot appears in the EL transient, indicating that the device response is no longer governed only*
250 *by the onset of carrier injection. Instead, longer electrical excitation allows a more developed space-*
251 *charge distribution to form within the PeLED, which modifies the internal field, carrier balance, and*
252 *recombination dynamics. The appearance of this overshoot therefore marks the transition towards a*
253 *more quasi-stationary operating regime, where the EL depends not only on injection but also on the*
254 *redistribution of accumulated charge inside the device. To isolate the effect of IR-assisted carrier*
255 *injection, the pump–push EL measurements were therefore performed using short electrical pulses,*
256 *where the device response is less affected by slow space-charge redistribution.*

257

258

259

260

261

262

263

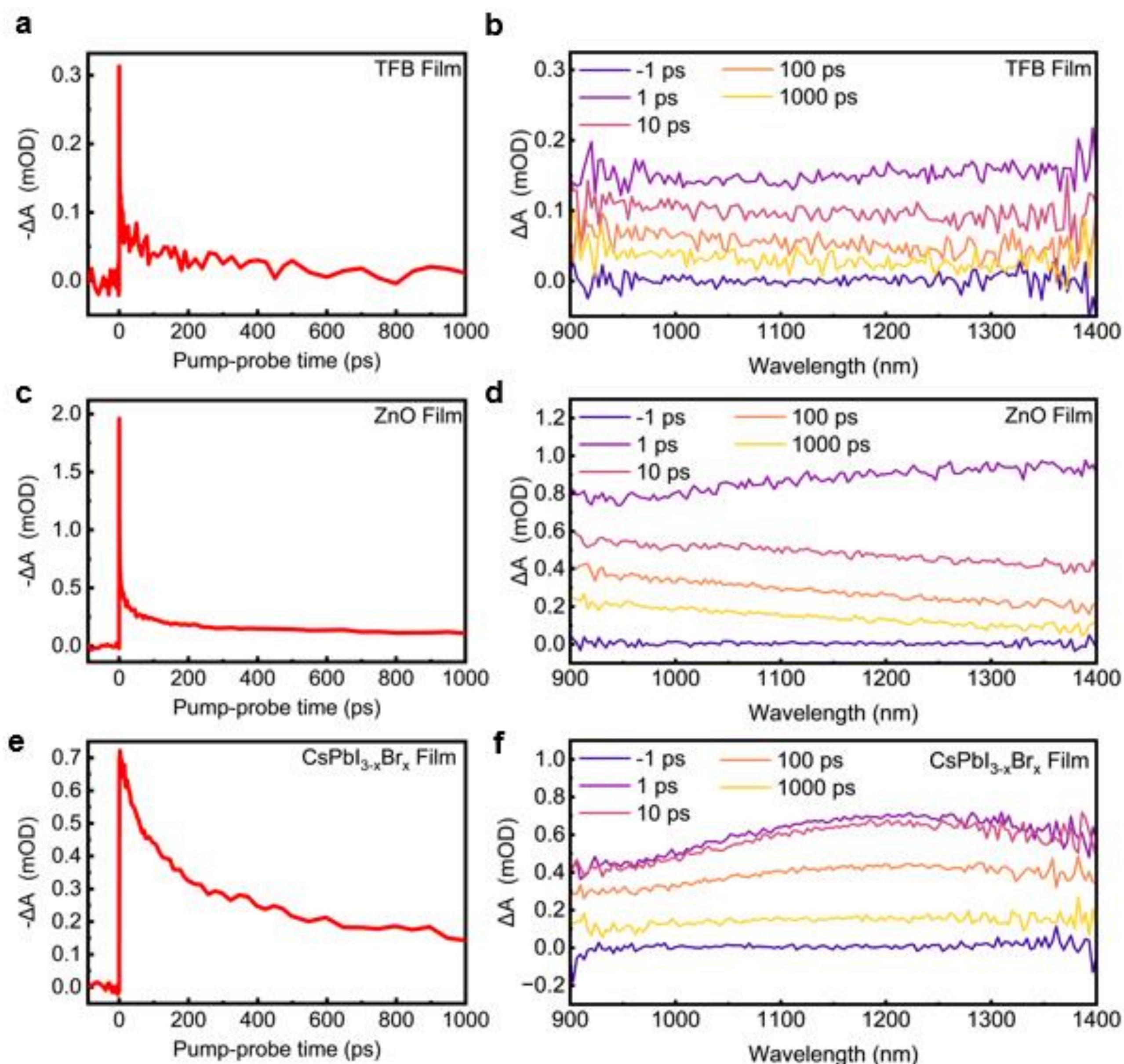

264

265 ***Figure S17. fs-TAS on TFB, ZnO and $CsPbI_{3-x}Br_x$ films.*** *For the measurement of TFB film, the*
266 *pump light has a wavelength of 350 nm and a fluence of 0.12 mJ cm^{-2}. For the measurement of ZnO*
267 *film, the pump light has a wavelength of 350 nm and a fluence of 0.73 mJ cm^{-2}. For the measurement*
268 *of $CsPbI_{3-x}Br_x$, the pump wavelength is 450 nm with a fluence of 20.7 μJ cm^{-2}.*

269

270

271

272

Supplementary Note 2. Simulation Result

Fig. S18 shows the simulated spatiotemporal maps of the electron and hole densities in the Au/TFB/$CsPbBrI_2$/ZnO/ITO perovskite LED device during a 100 ns electrical pulse, with and without IR push. The spatial coordinate is defined from the Au/TFB side to the ZnO/ITO side, with the TFB/EML and EML/ZnO interfaces located at 80 and 155 nm, respectively. Under electrical excitation, the carrier distribution is strongly shaped by the charge-selective transport layers and by the finite, bias-dependent carrier transfer across the TFB/EML and EML/ZnO interfaces. Electrons injected from the ITO electrode into the ZnO accumulate primarily within ZnO side and near the EML/ZnO interface, forming an electron-rich space-charge reservoir adjacent to the EML. Holes injected from the Au electrode into the TFB hole-transport layer accumulate primarily within TFB and near the TFB/EML interface, forming a hole-rich region adjacent to the emissive layer. Thus, before the arrival of the IR push, the device is characterized not by a spatially homogeneous electron-hole population, but by a dynamically established interfacial carrier distribution. Radiative recombination occurs primarily in regions where electrons supplied from the ITO/ZnO side overlap with holes supplied from the Au/TFB side.

Comparison of the electron-density maps with and without the IR push reveals that the push pulse produces a localized and prompt perturbation of the electron population close to the EML/ZnO interface (**Fig. S18a, b**). This perturbation appears at the push arrival time and subsequently redistributes into the perovskite layer on the nanosecond timescale. Importantly, the corresponding hole-density maps are nearly unchanged by the IR push (**Fig. S18c, d**). The simulated response therefore does not require the IR pulse to create a new hole population or to globally modify hole injection from the TFB side. Instead, the IR push selectively mobilizes the pre-existing electron-side space-charge reservoir near the EML/ZnO interface, which consists of both mobile electrons and trapped electrons in the ZnO-side interfacial region. Once released from interfacial traps or driven across the interface into the adjacent perovskite region, these additional electrons overlap with the pre-established hole population in the EML. Because the local radiative recombination rate scales as $R_{\mathrm{rad}} = Bnp$, a spatially localized increase in n can produce a measurable transient enhancement of EL without a comparable perturbation in p. Within this framework, the prompt ΔEL component is assigned to the immediate enhancement of local bulk radiative recombination within the EML adjacent to the EML/ZnO interface. The slower ΔEL component reflects the subsequent transport-driven redistribution of the same push-mobilized electrons within the EML, rather than delayed hole generation or a separate balanced carrier-generation process.

306 The late-time relaxation after the electrical pulse is governed by stored charge rather than by an
307 instantaneous removal of carriers at the external voltage turn-off. In the simulation, the falling edge
308 of the applied pulse is treated as a finite internal-voltage relaxation, and the contact and interfacial
309 carrier-exchange terms are smoothly reduced as the internal device voltage decays. Physically, this
310 treatment represents the combined effects of device capacitance, finite RC discharge, interfacial
311 barriers, and the incomplete extraction of accumulated carriers immediately after the external bias is
312 removed. This voltage-retention treatment prevents an unphysical abrupt reset of the carrier densities
313 at the end of the voltage pulse, while preserving the same boundary conditions for the with-push and
314 without-push simulations. Therefore, the differential feature induced by the IR push remains
315 attributable to the selective mobilization and redistribution of the electron-side space-charge reservoir,
316 rather than to a change in the electrical driving waveform.

317 Together, these simulations provide a mechanistic picture for the push-induced EL enhancement.
318 During the electrical pulse, an electron-rich reservoir builds up near the EML/ZnO interface because
319 electron injection from the ITO/ZnO side and subsequent interfacial transfer into the perovskite are
320 not instantaneously balanced by radiative recombination and carrier extraction. The IR push
321 transiently mobilizes part of this stored electron population and drives additional electrons into the
322 adjacent EML region, where holes have already penetrated from the TFB side. This produces a prompt
323 increase in local bulk radiative recombination near the EML/ZnO interface, followed by a slower
324 component associated with transport-driven redistribution of the same push-mobilized electrons
325 within the EML. The absence of a corresponding perturbation in the hole-density maps supports an
326 electron-dominated push response, consistent with the interpretation that the IR push primarily
327 mobilizes stored electron-side charge rather than directly generating a spatially balanced electron-
328 hole population throughout the perovskite layer.

329

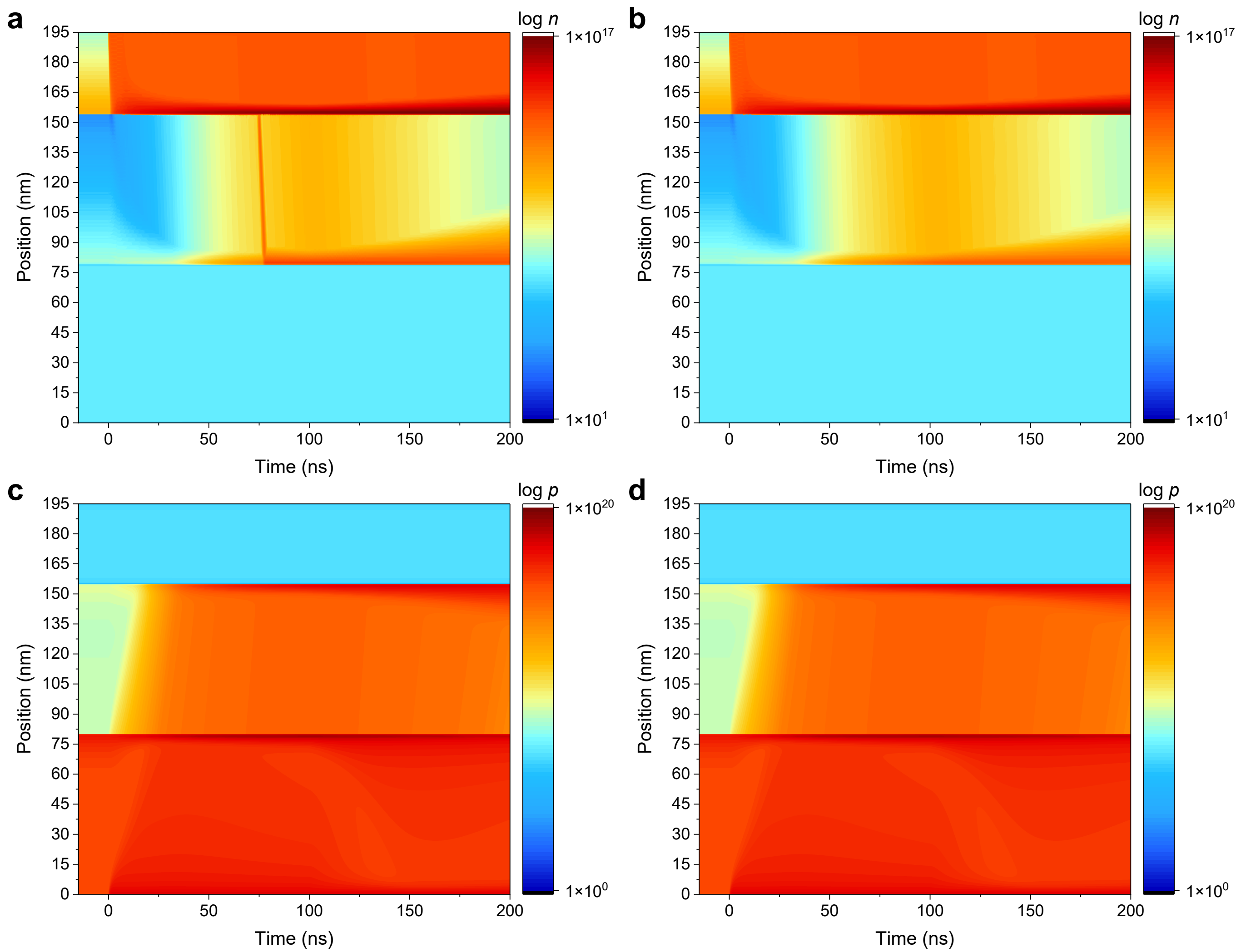

330 **Figure S18. Simulated spatiotemporal carrier-density maps in the Au/TFB/$CsPbBrI_2$/ZnO/ITO**
331 **device under electrical excitation, with and without the IR push pulse.** (**a**) Simulated electron-
332 density map, log *n*, with push. (**b**) Simulated electron-density map, log *n*, without push. (**c**) Simulated
333 hole-density map, log *p*, with push. (**d**) Simulated hole-density map, log *p*, without push. The spatial
334 coordinate *x* runs from the Au/TFB side to the ZnO/ITO side, with the TFB/EML and EML/ZnO
335 interfaces located at 80 and 155 nm, respectively. The device is driven by a 5 V forward-bias pulse
336 starting at 0 ns and ending at 100 ns.

337

338 **Supplementary Note 3. Self-Consistent Full-Device Drift-Diffusion Model for Push-Assisted**
339 **Charge Injection and the Δ*EL* Response**

340 To interpret the operando electrically-pump, IR-push-induced change in electroluminescence
341 (ΔEL), we developed a self-consistent one-dimensional full-device model for the
342 Au/TFB/$CsPbBrI_2$/ZnO/ITO device. The model resolves the hole transport layer (HTL), perovskite
343 emissive layer (EML), and electron transport layer (ETL) explicitly and solves coupled Poisson, drift-
344 diffusion, contact-exchange, heterojunction-transfer, and interfacial-trap equations. In this model, the
345 IR push acts on electron-side space charge accumulated near the EML/ETL interface, including both
346 accumulated mobile electrons in the near-interfacial ETL region and trapped electrons in an interfacial
347 trap manifold. The push transiently mobilizes these pre-existing electrons and injects them into the
348 EML close to the interface. As a result, the prompt ΔEL component is assigned to an immediate
349 increase in local bulk recombination near the EML/ETL interface, while the slower component
350 reflects the subsequent transport-driven redistribution of the same push-released electrons within the
351 EML.

352 1. Device Structure and Simulation Setup

353 The simulated device consists of three spatially resolved semiconductor layers: TFB (HTL; 80 nm),
354 $CsPbBrI_2$ (EML; 75 nm), and ZnO (ETL; 40 nm), sandwiched between an Au anode (work function
355 5.30 eV) and an ITO cathode (work function 4.60 eV). The built-in potential is set by the contact
356 work-function difference. The spatial coordinate x is defined across the device thickness from the
357 Au/HTL side to the ETL/ITO side. In the transient simulation, the device is driven by a 5 V forward-
358 bias pulse of 100 ns duration, and the infrared push is modeled as a 1064 nm Gaussian pulse centered
359 at 65 ns with a full width at half maximum of 0.6 ns. Prior to the transient calculation, the device is
360 relaxed to zero-bias equilibrium, ensuring that the electrical pulse is applied to a self-consistent
361 stationary state rather than to an arbitrary initial carrier distribution. Carrier-map calculations are
362 performed using Δx = 2.5 nm and Δt = 0.01 ns.

363 2. Governing equations

364 Carrier transport was solved self-consistently together with Poisson's equation across the complete
365 multilayer device. The electrostatic potential $\phi(x,t)$ satisfies:

366
$$\frac{\partial}{\partial x}\left[\varepsilon(x)\frac{\partial \phi(x,t)}{\partial x}\right] = -q[p(x,t) - n(x,t) - n_t(x,t)] \quad (1)$$

367 where $n(x,t)$ and $p(x,t)$ are the mobile electron and hole densities, respectively, $n_t(x,t)$ is the total
368 trapped-electron density, $\phi(x,t)$ is the electrostatic potential, and $\varepsilon(x)$ is the position-dependent
369 permittivity.

370 The mobile carriers obey the continuity equations:

371 $$\frac{\partial n}{\partial t} = -\frac{\partial \Gamma_n}{\partial x} - B_{\mathrm{rad}}(x)\, n(x,t)\, p(x,t) - C_{\mathrm{trap}} + R_{\mathrm{th}} - S_{\mathrm{push,free}} + S_{\mathrm{push,inj}} \quad (2)$$

378 $$\frac{\partial p}{\partial t} = -\frac{\partial \Gamma_p}{\partial x} - B_{\mathrm{rad}}(x)\, n(x,t)\, p(x,t) \quad (3)$$

372 where Γ_n and Γ_p are the electron and hole fluxes, respectively. $B_{\mathrm{rad}}(x)$ is the bimolecular radiative
373 recombination coefficient, taken to be nonzero only within the perovskite EML. C_{trap} describes free-
374 electron capture into the interfacial trap manifold, whereas R_{th} represents thermal release from the
375 same manifold. $S_{\mathrm{push,free}}$ accounts for the push-induced removal of mobile electron-side space
376 charge from the ETL region, and $S_{\mathrm{push,inj}}$ represents reinjection of the total push-released charge into
377 the EML through a near-interface source term.

379 The transport fluxes were evaluated using the Scharfetter-Gummel discretization with layer-
380 dependent mobilities and transport potentials. This discretization is widely used for semiconductor
381 drift-diffusion calculations because it remains numerically stable under conditions of strong
382 electrostatic gradients and heterojunction energy offsets. For electrons, the transport potential was
383 written as $\psi_n = \phi + \chi + V_T \ln(N_C)$, whereas for holes it was written as $\psi_p = \phi + IP - V_T \ln(N_V)$,
384 where χ is the electron affinity, IP is the ionization potential, and $V_T = k_B T/q$. This formulation
385 provides stable carrier fluxes across the multilayer device and avoids numerical artifacts at material
386 interfaces.

387 3. Contacts, heterojunction transfer, voltage-dependent retention, and 388 equilibrium initialization

389 The metal contacts were modeled as finite-rate carrier-exchange boundaries rather than ideal
390 reservoirs with fixed carrier densities. Under forward bias, hole exchange at the Au/TFB contact and
391 electron exchange at the ZnO/ITO contact dominate the injection response, whereas the
392 corresponding minority-carrier exchange terms were retained to allow finite leakage-like exchange
393 and to avoid singular boundary conditions. The contact exchange fluxes were scaled by the
394 instantaneous internal device voltage, so that carrier exchange with the electrodes decreases
395 continuously as the device discharges after the electrical pulse. This treatment avoids an unphysical

396 abrupt reset of the carrier densities at the voltage turn-off and allows accumulated carriers to relax
397 through finite recombination, transport, and extraction processes.

398 Carrier transfer across the TFB/EML and EML/ZnO heterojunctions was described by explicit field-
399 assisted interfacial transfer terms in addition to the Scharfetter-Gummel drift-diffusion fluxes within
400 each layer. At the TFB/EML interface, hole transfer from TFB into the EML was governed by a finite
401 transfer velocity and an effective barrier associated with the ionization-potential offset. At the
402 EML/ZnO interface, electron transfer from ZnO into the EML was treated analogously using a finite
403 electron-transfer velocity and the conduction-band offset. In both cases, the interfacial electric field
404 reduces the effective transfer barrier through a phenomenological field-assistance term, $\Delta E_{\mathrm{field}} =$
405 $\beta\sqrt{E_{\mathrm{int}}}$, where β is an empirical field-assistance parameter and E_{int} is the local interfacial electric
406 field. This formulation captures the enhanced cross-interface carrier transfer under forward bias
407 without assigning a unique microscopic hopping mechanism.

408 To account for finite post-pulse charge retention in the multilayer LED stack, a voltage-dependent
409 retention factor was introduced as

410 $$G_V(t) = clip[k_V V_{int}(t),0,1]$$

411 where $V_{int}(t)$ is the internal device voltage and k_V is a phenomenological voltage-scaling factor. This
412 retention factor was used to scale contact exchange and voltage-assisted interfacial carrier exchange,
413 and to suppress carrier outflow from the EML into the adjacent transport layers as the internal voltage
414 decays. Physically, $G_V(t)$ represents the combined effect of finite device capacitance, interfacial
415 barriers, and incomplete carrier extraction immediately after the external bias is removed. It is not a
416 carrier-generation term and is applied identically to the simulations with and without the IR push;
417 therefore, the calculated differential EL response arises from the push-induced redistribution of stored
418 electron-side charge rather than from a change in the electrical driving waveform.

419 Before the transient simulation, the device was relaxed at zero applied bias until the coupled carrier,
420 trapped-charge, and electrostatic-potential distributions converged to a stationary state. The forward-
421 bias pulse therefore builds interfacial space charge on top of a self-consistent initial electrostatic and
422 trap occupation profile. This initialization is important because the pre-existing built-in potential and
423 trap population influence the formation of the electron-side space-charge reservoir once the electrical
424 pulse is applied.

425

426

4. Interfacial trap manifold and push-assisted space-charge mobilization

A push-active interfacial trapped-electron reservoir was introduced on the EML/ETL side of the device, extending over the first 6 nm within the ETL side of the heterojunction. In the simplified model, the interfacial trapped charge was represented by a single effective trap population $n_t(x, t)$, rather than by a distributed trap density of states. The occupancy of this effective trapped-electron reservoir evolved according to:

$$\frac{\partial n_t}{\partial t} = C_{\mathrm{trap}} - R_{\mathrm{th}} - R_{\mathrm{push}} \quad (4)$$

where C_{trap} denotes capture of free electrons into the available trap population, R_{th} denotes thermal release from the same reservoir, and R_{push} denotes push-induced optical release. In this effective description, the interfacial trapped electrons serve as a pre-accumulated electron-side space-charge reservoir without introducing an explicit distribution of trap depths. The push pulse does not generate an independent carrier population. Instead, it acts on electron-side space charge that has already been established during the electrical pulse. Within this framework, a single optical event mobilizes two pre-existing electron reservoirs: (i) trapped electrons in the interfacial trap reservoir and (ii) mobile electrons in the near-interfacial ETL region. For the trapped contribution, the instantaneous push-induced release rate is written as:

$$R_{\mathrm{push}}(x, t) = \nu_{\mathrm{push}}^{0}\, g_{\mathrm{push}}(t)\, w_x^{\mathrm{push}}\, n_t(x, t) \quad (5)$$

where $g_{\mathrm{push}}(t)$ is the normalized Gaussian temporal profile of the push pulse, ν_{push}^{0} is the peak optical release rate, and w_x^{push} is the spatial weighting factor that imposes the decay of the push-active interfacial region.

For the mobile-electron contribution, the model integrates the pre-existing near-interfacial ETL electron space charge using an exponentially decaying spatial weight on the ETL side. The push converts this mobile space-charge reservoir into an injected electron flux through an effective mobilization velocity. The mobile and trapped push-released contributions are then combined into a total injection flux:

$$\Phi_{\mathrm{push,total}}(t) = \Phi_{\mathrm{push,free}}(t) + \Phi_{\mathrm{push,trap}}(t) \quad (6)$$

which is deposited directly into the EML through a normalized near-interfacial source profile:

455 $$S_{\text{push,inj}}(x,t) = \Phi_{\text{push,total}}(t)\ \exp\left[\frac{x_{\text{int}} - x}{\lambda_{\text{push}}}\right] \quad (7)$$

456 where x restricted to the EML side of the EML/ETL interface. x_{int} is the position of the EML/ETL
457 interface, and λ_{push} is the characteristic decay length of the push-induced injection profile. Within
458 this framework, the same push event both depletes electron-side space charge from the ETL side and
459 reinjects the released charge into the adjacent EML region. No separate interfacial emissive state is
460 introduced. The prompt rise in ΔEL is therefore attributed to the immediate enhancement of local bulk
461 recombination in the near-interfacial EML region, whereas the delayed component reflects the
462 subsequent redistribution of the same push-released electrons through the perovskite layer.

463

464 **5. Signal construction, fitting protocol, and diagnostics**

465 The raw electroluminescence was calculated from the spatially integrated bimolecular radiative
466 recombination rate:

467 $$EL_{\text{raw}}(t) = \int B_{\text{rad}}(x)\, n(x,t)\, p(x,t)\, dx \quad (8)$$

468 where $B_{\text{rad}}(x)$ is the local bimolecular radiative recombination coefficient and $n(x,t)$ and $p(x,t)$
469 are the local mobile electron and hole densities. Because $B_{\text{rad}}(x)$ was set to zero in the HTL and ETL,
470 the integral effectively reduces to the perovskite EML. The experimentally observable signal was
471 then obtained by convolving $EL_{\text{raw}}(t)$ with a normalized Gaussian photomultiplier response function
472 $G_{\text{PMT}}(t)$ with a full width at half maximum of 5 ns:

474 $$EL_{\text{meas}}(t) = EL_{\text{raw}}(t) * G_{\text{PMT}}(t) \quad (9)$$

473 The push-induced electroluminescence change was defined as:

475 $$\Delta EL(t) = EL_{meas,with\ push}(t) - EL_{meas,no\ push}(t) \quad (10)$$

476 where the two measured EL traces correspond to simulations performed with and without the
477 infrared push pulse.

478

479

480

481

482

483 ## 6. Fixed device parameters used in the simulation

484 **Table S1. Fixed layer properties used in the full-device simulation.**

Layer	Thickness (nm)	ε_r	μ_n ($cm^2\ V^{-1}\ s^{-1}$)	μ_p ($cm^2\ V^{-1}\ s^{-1}$)	N_c (cm^{-3})	N_v (cm^{-3})
TFB (HTL)	80.0	3.5	1.0×10^{-7}	2.0×10^{-3}	1.0×10^{20}	1.0×10^{20}
$CsPbBrI_2$ (EML)	75.0	11.0	5.0×10^{-2}	5.0×10^{-3}	3.0×10^{18}	3.0×10^{18}
ZnO (ETL)	40.0	8.3	3.0×10^{-2}	1.0×10^{-8}	4.0×10^{18}	4.0×10^{18}

485

486

487 **Table S2. Fixed experimental timing and numerical settings used in the transient simulations.**

Quantity	Value
Time window	-50 to 250 ns
Electrical pulse	5 V rectangular pulse, 100 ns duration
Push pulse	1064 nm; center at 75 ns; 0.6 ns FWHM
PMT response	Gaussian, 5 ns FWHM
Space-charge integration window	±6.8 nm around each interface
Final carrier-map mesh / time step	Δx = 1 nm; Δt = 0.01 ns
Zero-bias equilibration	Iterative relaxation before transient run

488

489

490